Charge transfer induced energy storage in CaZnOS:Mn − insight from experimental and computational spectroscopy

Electronic supplementary information

Jonas J. Joos,*[ab] Kurt Lejaeghere,[c] Katleen Korthout,[ab] Ang Feng,[ab]
Dirk Poelman[ab] and Philippe F. Smet*[ab]

[a]LumiLab, Department of Solid State Sciences, Ghent University, Gent, Belgium
[b]Center for Nano- and Biophotonics (NB Photonics), Ghent University, Gent, Belgium.
[c]Center for Molecular Modeling (CMM), Ghent University, Gent, Belgium.

E-mail: jonas.joos@UGent.be, philippe.smet@UGent.be

S1   Computational method

S1.1   Density functional theory

The band structure of the host material and the impurity levels introduced by the defect were calculated in the framework of density functional theory (DFT). The projector-augmented wave (PAW) method was used as implemented in the Vienna Ab Initio Simulation Package (VASP)[1–3]. For the O and S atoms, the ns^2np^4 electrons were considered as valence electrons, while for Ca and Zn, these were $3s^23p^64s^2$ and $3d^{10}4s^2$ respectively. For Mn, the $3p^64s^23d^5$ electrons were explicitly accounted for as valence electrons. These settings correspond to the VASP 5.2 recommended potentials, which were shown to yield an excellent precision in comparison to all-electron codes[4,5]. A generalized gradient approximation (GGA) was utilized in the form of the Perdew-Burke-Ernzerhof (PBE) functional[6], supplemented by an on-site Coulomb interaction, parameterized according to a Hubbard Hamiltonian[7]. This additional interaction is known to improve the description of electron correlation effects within the 3d shells of Zn and Mn. The scheme of Dudarev was applied, i.e. using an effective Hubbard parameter, $U_{eff} = U − J$[8]. The choice for the empirical parameter U_{eff} was based on existing literature for similar systems, i.e. U_{eff}(Zn, 3d) = 7 eV was chosen, based on DFT+U calculations on ZnS[9–12] while U_{eff}(Mn, 3d) = 3 eV was chosen, based on DFT+U calculations on MnS, MnO and ZnO:Mn[13–16].

For all calculations, an energy cut-off of 650 eV and a 9x9x3 Monkhorst-Pack k-point grid[17] for a single CaZnOS unit cell were chosen to achieve a numerical accuracy better than 0.2 meV for the total energy. In addition, the grid settings for Fast Fourier Transforms were set to "Accurate", corresponding to grid spacings of $1/2G_{max}$ (or $1/4G_{max}$ for augmentation charges and charge densities), with G_{max} the maximum wave vector described by the basis set. Electronic smearing was treated using the Gaussian scheme[18,19] in relaxation runs (using a smearing width of 0.2 eV) and using the tetrahedron method by Blöchl for single point calculations[20]. Defective CaZnOS crystals were modeled by means of a supercell containing one defect. The supercell size was chosen by trading off the required computational resources and the convergence of the Kohn-Sham density of states (DOS) and defect formation energy. From this analysis, a 3x3x1 supercell containing 72 atoms was deemed to yield sufficiently accurate results for the calculated physical quantities (e.g. convergence of the defect formation energy up to 5 meV). This particular supercell dimension has the advantage that the separation between impurities in neighboring supercells is very similar along different directions, given the experimental lattice parameters of $a = b = 3.76$ Å and $c = 11.40$ Å. A 3x3x3 Monkhorst-Pack grid was selected to sample k-space for the supercells.

Starting from the experimentally determined crystal structure[21], the geometric optimization of the cells and supercells was performed for a series of fixed volumes, to which a Birch-Murnaghan equation of state was fitted to obtain the equilibrium cell volume[22,23]. Seven single-point calculations were used, distributed in an interval of 12% of the equilibrium volume around the equilibrium volume. Phonon calculations were performed by means of the phonopy package[24]. Finite displacements of 0.01 Å were applied to all atoms in the 3x3x1 Mn-doped supercell. The dynamical matrix was constructed from the corresponding forces. The eigenvalues of this matrix correspond to the phonon frequencies, which were plotted in density of states (DOS) plots with a

smearing width of $6\,\text{cm}^{-1}$ (0.18 THz). When considering a supercell of double that size, changes in the phonon frequencies were only of the order of $1\,\%$.

The work function was calculated for the surface orientation with the lowest surface energy by considering a slab model with 32 atomic layers and a vacuum separation of 47 Å. In addition, the non-centrosymmetric nature of the slab required correcting for its dipole moment. Such settings enable an optimal comparison to experiment. To combine the vacuum potential of the slab model with the Fermi energy of the bulk material, the method of macroscopic averages according to C. J. Fall *et al.* was used[25].

Impurity levels, induced by a defect X, in host crystal A, can be calculated from DFT by considering the defect formation energy, defined as[26–28]:

$$E^f(A:X^Q) = E_{\text{tot}}(A:X^Q) - E_{\text{tot}}(A) - \sum_i n_i \mu_i + Q(E_F + E_V + \Delta V). \tag{S1}$$

Herein, Q denotes the Kröger-Vink charge state of the defect and E_{tot} is the total energy of the supercell. The integer n_i indicates the number of atoms of type i that have been added ($n_i > 0$) or removed ($n_i < 0$) to form the defect and μ_i are the atomic chemical potentials. Finally, E_F is the Fermi energy, i.e. the electron chemical potential at absolute zero, referred with respect to the valence band maximum, E_V. An additional correction term, ΔV, based on the crystal potential, was added to Eq. S1 to align the energy reference for all calculations in accordance with the undoped cell[29].

In order to simulate the different charge states of the defects, electrons were added or removed from the supercell. To maintain a charge-neutral system, a homogeneously distributed background charge was added, compensating for the added or removed electrons. A monopole-monopole correction term was taken into account to correct the total energies for unphysical interaction between the defect and its periodic images, using the macroscopic dielectric constant of the host material calculated with density functional perturbation theory.

The impurity levels are defined as the so-called charge-state transition levels, i.e. the Fermi level locations at which two charge states of the defect have the same formation energy:

$$\varepsilon(Q/Q') = \frac{1}{Q-Q'} \left(E^f(A:X^{Q'})\big|_{E_F=E_V} - E^f(A:X^Q)\big|_{E_F=E_V} \right). \tag{S2}$$

These levels correspond to the experimental impurity levels which can be assessed through deep-level transient spectroscopy (DLTS) or charge-transfer (CT) luminescence. This is in sharp contrast to the Kohn-Sham levels originating from the defect and which emerge in the band gap[28]. These are not directly applicable to spectroscopy as total energies are required to describe experimental transitions. The above methodology was validated for various types of defects in diverse compounds[16,30,31].

To handle both the inaccuracy of the band gap energy determined by PBE+U as well as the dependence of the band gap energy and impurity level locations on the U_{eff} parameters, an extrapolation scheme was proposed by Janotti and Van de Walle for the LDA+U functional[32]. Here, we applied this scheme to the PBE+U functional. In this extrapolation scheme, physical impurity level locations are obtained by shifting formation energies according to the differences between the PBE and PBE+U band gap on one hand and the experimental band gap and the PBE+U band gap on the other hand[32]:

$$E^f(A:X^Q) = E^{f,\text{PBE}+U}(A:X^Q) + \frac{E_G^{\text{exp}} - E_G^{\text{PBE}+U}}{E_G^{\text{PBE}+U} - E_G^{\text{PBE}}} n\Delta\bar{\varepsilon}. \tag{S3}$$

Here, n is the single particle occupation number of the defect states in the band gap for charge state Q and $\Delta\bar{\varepsilon}$ is the difference for the $\varepsilon(Q/Q')$ values, calculated with PBE+U and PBE, averaged over the available charges Q'. A good correspondence between these extrapolated impurity levels and the experimental levels has been shown for multiple examples[28,32,33].

S1.2 Crystal field theory

Crystal field theory (CFT) considers the luminescent defect from an atomic point of view where the host crystal is considered as a perturbation, shifting and splitting the atomic multiplets[34]. An effective Hamiltonian is diagonalized which is a sum of different terms, accounting for the different interactions. Each term is factorized as a radial integral, which is obtained empirically, and an angular integral, which is exactly calculated by algebraic methods, based on irreducible tensor operators, following the approach by Racah[35–38]. Given the limited number of transitions found in experimental spectra, only the most important interactions can be accounted for:

$$
\begin{aligned}
\mathcal{H} &= E_0 + \sum_{k=2,4} f_k F^k + \sum_{i=1}^{N} \sum_{k=2,4} \sum_{q=0}^{k} B_{kq} \left(C_{kq}(i) + (-1)^q C_{k\,-q}(i) \right) \\
&\quad + \zeta_{3\mathrm{d}} A_{\mathrm{so}} + \alpha L(L+1) + \beta Q.
\end{aligned}
\tag{S4}
$$

The first term contains the spherically symmetric contributions of all interactions. In practice, the calculated energy spectrum is shifted to put the lowest eigenenergy at zero. Furthermore, the F^k are Slater-Condon parameters, describing the non-central part of the inter-electronic Coulomb repulsion. As an alternative to F^2 and F^4, the Racah parameters B and C are often used[36]. B_{kq} are the single-particle crystal field (CF) parameters[34]. The point symmetry of the system and angular momentum selection rules dictate which B_{kq}'s are nonzero[34,39]. The three last terms improve the description of experimental spectra and are quantified through the spin-orbit constant $\zeta_{3\mathrm{d}}$ and Trees coefficients α and β respectively[40,41]. f_k, C_{kq}, A_{so}, $L^2/\hbar^2$ (with eigenvalues $L(L+1)$) and Q are the associated irreducible tensor operators. The operator C_{kq} is proportional to the spherical harmonics ($C_{kq} = \sqrt{4\pi/(2k+1)} Y_{kq}$) and Q is Racah's seniority operator[38]. The last two terms in Eq. S4 account for configuration interactions in an effective way[42,43].

Electron correlation effects in Eq. S4 are restricted to the same two terms as in the atomic case. However, in non-spherical crystal fields, a large number of two-electron operators can be added to $\mathcal{H}$ without violating symmetry constraints[44,45]. The total number of parameters for the correlation crystal field can be restricted via the so-called spin-correlated crystal field (SCCF) Hamiltonian,

$$
\mathcal{H}_{\mathrm{sccf}} = \sum_{i=1}^{N} \sum_{k=2,4} \sum_{q=0}^{k} c_k B_{kq}\, s_i \cdot S \left(C_{kq}(i) + (-1)^q C_{k\,-q}(i) \right),
\tag{S5}
$$

which captures the spin-dependent Coulomb exchange part of the correlation effect upon adding only two parameters c_k[45–47]. The s_i denote the spins of the individual electrons while S is the total spin of the electron configuration. Eq. S5 was originally introduced by Judd to improve the description of lanthanide spectra, but can equally well be applied to transition metal spectra[48,49].

The CF calculations were performed with an in-house developed Python program which calculates matrix elements of Eqs. S4 and Eq. S5, diagonalizes the Hamiltonian and searches optimal values* for the empirical radial integrals through a downhill-simplex algorithm[50,51]. A Russell-Saunders $^{2S+1}L_{J(M_J)}$ basis was used, which is 252 dimensional in the case of a d^5 configuration.

---

* Corresponding to a minimal deviation between experimental and calculated energies, $\sigma_{\mathrm{CF}} = \sqrt{\frac{\Sigma_i (E_i^{\mathrm{exp}} - E_i^{\mathrm{calc}})^2}{N-P}}$ for N levels of a manifold, using P empirical parameters.

S2 Formation energy of CaZnOS

It is known that the quaternary compound CaZnOS is unstable at high temperature. The competitive reaction $ZnS + CaO \rightleftharpoons CaS + Zn + 0.5\,O_2$, which is the principle to recycle Zn in industry, is unavoidable, especially in a reducing atmosphere. This results in impurities, mainly of the binary compounds ZnS, CaS and CaO[52,53]. This finding is reflected in the formation energy of the compound which was calculated with respect to the experimental precursors ZnS and CaO. While PBE yields a positive value of 39 meV per formula unit, corresponding with an unstable CaZnOS phase, PBE$+U$ yields a negative value of -16 meV per formula unit. These small numbers support the empirical finding of most experimental studies -including this one- that it is hard to obtain phase-pure CaZnOS. Small contaminations of binary by-products are always found in PXRD patterns before post-treatments. Nevertheless, the stability of synthesized CaZnOS was positively validated at room temperature through PXRD and luminescence spectroscopy of doped samples over time.

S3 Low symmetry and spin-correlated crystal fields for CaZnOS:Mn^{2+}

In this supplementary section, the effects of two additional terms in the crystal field Hamiltonian on the spectrum of Mn^{2+} in CaZnOS is discussed. First, the low symmetry component of the crystal field is considered. Subsequently, the effect of non-spherically symmetric electron correlation is demonstrated. It will be shown that the latter contribution is more important to achieve a good fit to the experimental photoluminescence spectrum. The former contribution can then be neglected to keep the number of empirical parameters in the effective Hamiltonian limited.

The coordination polyhedron for Mn^{2+}, when incorporated on a Zn site is not perfectly T_d symmetric, but the mixed anionic nature of the compound results in a lower C_{3v} symmetry. This has two repercussions on the crystal field (CF) parameterization, i.e. the tetrahedral ratio between B_{40} and B_{43} ceases to hold and another nonzero parameter, B_{20}, emerges, yielding a total of three independent CF parameters. Often, an alternative parameterization due to Ballhausen is used in this case[54]:

$$
\begin{aligned}
B_{20} &= -7D\sigma \\
B_{40} &= -14Dq - 21D\tau \\
B_{43} &= -2\sqrt{70}Dq.
\end{aligned}
\tag{S6}
$$

When using this notation, the lowering of symmetry is stressed through the deviation of the tetrahedral ratio ($D\tau \neq 0$) and the emergence of the additional term in the Hamiltonian ($D\sigma \neq 0$).

The additional terms in the CF Hamiltonian cause further splitting of the crystal field levels, i.e. the orbital triplets split in a doublet and a singlet, while the orbital doublets and singlets maintain their degeneracy. As the ^{4}G(T_1/T_2) terms feature broad excitation bands, their splitting is not visible. Different lines are resolved from excitation to the ^{4}D(T_2) term, but it is not possible to derive the splitting due to the symmetry lowering as the lines can also originate from vibronic side bands. At first sight, it therefore seems difficult to quantify the symmetry lowering in terms of crystal field parameters.

A straightforward explanation for the lifting of the accidental degeneracy of the $^4A_1$ and ^4E levels would be to attribute it to the symmetry lowering, offering a means to quantify $D\sigma$ and $D\tau$. Figure S1 compares the effect of the two additional crystal field parameters on the energy difference between $^4A_1$ and ^4E, denoted as $\Delta E(^4\Gamma)$, and on the energy of the lowest excited state, $E(^4T_1)$. As one can see from this figure, symmetry lowering alone cannot account for the degeneracy lifting as it requires unrealistically high values of $|10D\sigma|$ in the range of 25B, compared to typical $|10Dq|$ values in the range of $5-10B$ for tetrahedral Mn^{2+} complexes[55–58].

The accidental degeneracy of the $^4A_1$ and ^4E levels and its lifting - even in fields of T_d or O_h symmetry - has been the subject of long debate[49,58,59]. Koide and Pryce modeled this phenomenon by proposing non-equal Racah parameters for electrons in the e and t_2 orbitals, which they attributed to *covalency*. Ng and Newman showed that the assumptions of this so-called epsilon or renormalization model are in contradiction with two-electron
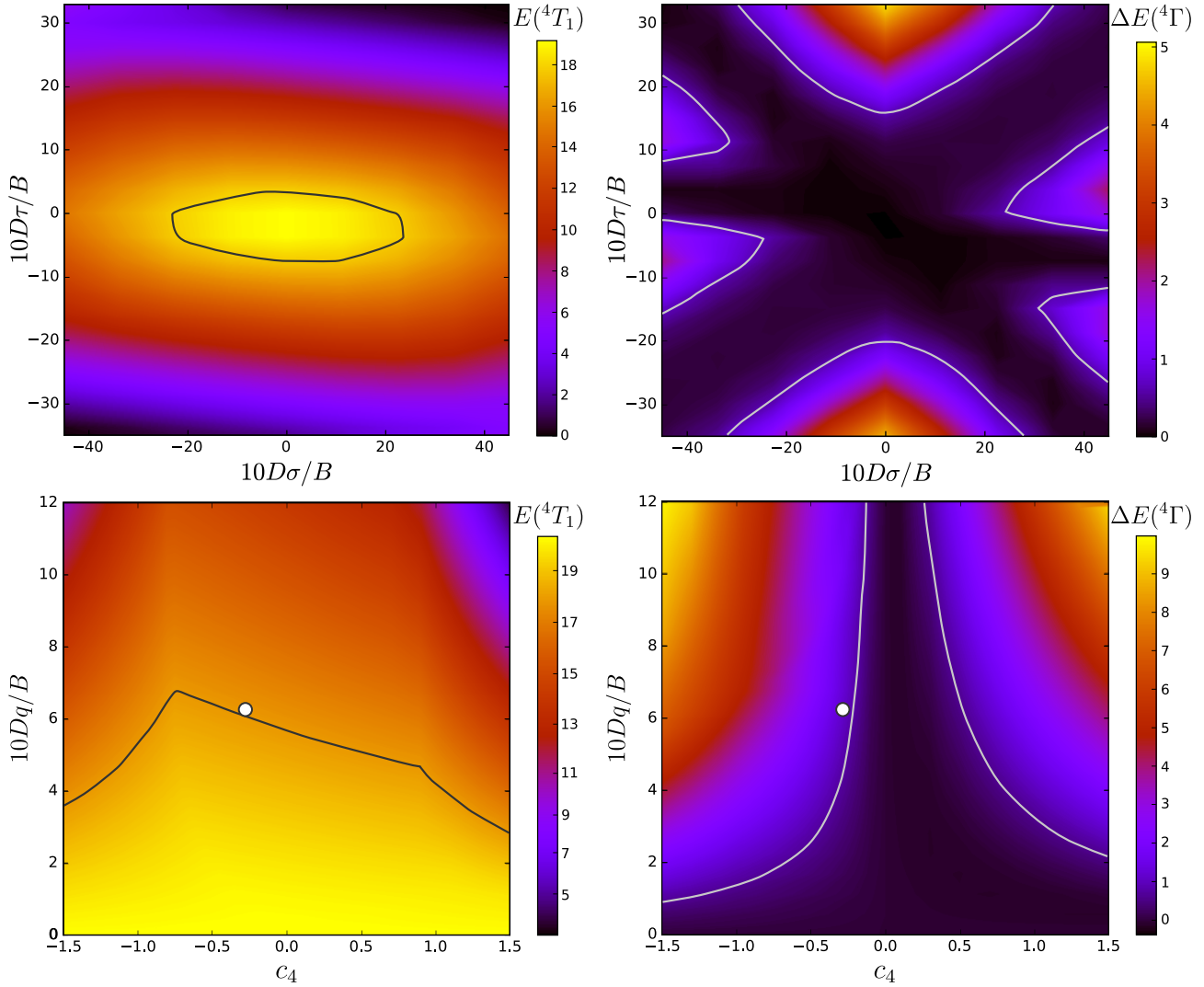
Figure S1 Energy of the emitting level, $E(^4T_1)$ (left) and the lifting of the accidental degeneracy, $\Delta E(^4\Gamma) = E(^4A_1) - E(^4E)$ (right), as a function of symmetry lowering, $10D\sigma$ and $10D\tau$ (top) and as a function of the spin-correlated crystal field, c_4 (bottom). The parameter values at which the experimental values for the displayed quantities are found, are marked by the black and white lines, the optimized parameter values by the white dot. All energy values in 1000 cm^{-1}.

integrals, calculated through a configuration interaction technique[60,61]. Subsequently, the same authors showed that an improved description of experimental spectra of octahedral Mn^{2+} ions in halides, corresponding with σ_{CF} values in the range of 290-770 meV, could be obtained by adding the spin-correlated crystal field, already known from lanthanide spectroscopy, Eq. S5, to the effective Hamiltonian[49].

In the high-symmetry case of T_d, only one additional parameter, c_4, is required. Upon lowering symmetry to C_{3v}, a second nonzero parameter, c_2, emerges. As crystal field studies have shown that the importance of c_k parameters increases with k, c_2 can be neglected at leading order, along with $D\sigma$ and $D\tau$[46]. In Fig. S1, it is shown that the experimental $^4A_1$ - ^4E splitting can be obtained together with a realistic value for the lowest excited state. Therefore, the spin-correlated crystal field term is used to describe the experimental spectrum. To reduce the number of fitting parameters, T_d symmetry is assumed, which is an acceptable simplification.

S4 Electron-phonon coupling

According to the Franck-Condon approximation, the intensity of the emission spectrum from eigenstate i to eigenstate f is proportional to the squared modulus of

$$\langle \psi_\mathrm{f} | D | \psi_\mathrm{i} \rangle \langle \chi_{\mathrm{f},N} | \chi_{\mathrm{i},N'} \rangle \tag{S7}$$

where the first factor is the electronic transition moment featuring D, the electrons' electric dipole moment in the case of electric dipole transitions (E1), and the second factor the Franck-Condon integral[62]. ψ and χ denote electronic and vibrational wave functions respectively.

The allowed or forbidden character of the transition can be assessed from the first factor in Eq. S7. Although intraconfigurational 3d transitions have a small transition probability, different mechanisms relax the selection rules. The tetrahedral coordination of the Mn ion does not possess a symmetry center whereby the Laporte parity selection rule does not hold and the intraconfigurational 3d transition can become symmetry allowed if the E1 selection rules $\Delta L = 1$, $\Delta S = 0$ are fulfilled. This seems not to be the case at first sight. However, the crystal field can mix some ^{4}P character in the ^{4}G eigenstate, relaxing the $\Delta L = 1$ rule. Furthermore, the $\Delta S = 0$ rule is relaxed by the spin-orbit interaction. The electronic transition moment $\langle ^6S(A_1) | D | {}^4G(T_1) \rangle$ can then be nonzero, evidenced by the occurrence of the totally symmetric irreducible representation (irrep) A_1 in the reduction of the direct product $A_1 \otimes T_2 \otimes T_1$, considering that the electric dipole moment transforms according to the irrep T_2. Additional contributions can originate from mixing with higher-lying excited states through the odd part of the crystal field.

The shape of an emission or excitation band is obtained by the second factor in Eq. S7. It shows how many quanta, i.e. phonons of every vibrational mode, are created or annihilated during the transition. When multiple vibrational modes are involved during an electronic transition, the standard Huang-Rhys theory for vibronic transitions involving one vibrational mode is not directly applicable. Liu et al. have proposed an extension of the low temperature limit of this theory for multiphonon vibronic spectra[63] inspired by the observation by Bron and Wagner that both local and lattice modes can couple to electronic transitions[64–66]. The spectral shape of an emission band is then given by the sum of two contributions:

$$
\begin{aligned}
I(E) \; = \; & I_{0,\mathrm{loc}} \sum_{N_k} \cdots \sum_{N_1} \left(\prod_{i=1}^{k} e^{-S_i} \frac{S_i^{N_i}}{N_i!} \right) \left(\frac{E_0 - \sum_{i=1}^{k} N_i \hbar \omega_i}{E_0} \right)^4 f \left(E; E_0 - \sum_{i=1}^{k} N_i \hbar \omega_i; \sigma \right) \\
& + I_{0,\mathrm{lat}} \sum_{N_k} \cdots \sum_{N_1} \sum_{N_\Omega} \left(\prod_{i=1}^{k} e^{-S_i} \frac{S_i^{N_i}}{N_i!} \right) \left(e^{-S_\Omega} \frac{S_\Omega^{N_\Omega}}{N_\Omega!} \right) \left(\frac{E_0 - \sum_{i=1}^{k} N_i \hbar \omega_i}{E_0} \right)^4 f \left(E; E_0 - N_\Omega \hbar \Omega - \sum_{i=1}^{k} N_i \hbar \omega_i; \sigma_\Omega \right).
\end{aligned}
\tag{S8}
$$

The first term contains the contributions of the k different local modes with suitable symmetry labels, characterized by frequency ω_i and electron-phonon coupling S_i. This term contains harmonic lines as well as lines originating from frequency mixing between the different modes. The lines are broadened by a Gaussian shape function $f(E; \mu; \sigma)$, centered at μ and having a width σ. E_0 denotes the energy of the ZPL. The second term originates from the coupling of Franck-Condon allowed modes to lattice acoustic modes[63]. This is modeled by a single average lattice phonon frequency Ω, coupled to all allowed local modes with an effective Huang-Rhys parameter S_Ω and a broad density of phonon modes, yielding $\sigma_\Omega \gg \sigma$[63]. The second term ensures a good fit of the broad band underlying the fine structure.

References

[S1] G. Kresse and J. Furthmuller, *Computational Materials Science*, 1996, **6**, 15–50.

[S2] G. Kresse and D. Joubert, *Physical Review B*, 1999, **59**, 1758–1775.

[S3] J. Hafner, *Journal of Computational Chemistry*, 2008, **29**, 2044–2078.

[S4] K. Lejaeghere, V. Van Speybroeck, G. Van Oost and S. Cottenier, *Critical Reviews in Solid State and Materials Sciences*, 2014, **39**, 1–24.

[S5] K. Lejaeghere *et al.*, *Science*, 2016, **351**, aad3000.

[S6] J. P. Perdew, K. Burke and M. Ernzerhof, *Physical Review Letters*, 1996, **77**, 3865–3868.

[S7] A. I. Liechtenstein, V. I. Anisimov and J. Zaanen, *Physical Review B*, 1995, **52**, R5467–R5470.

[S8] S. L. Dudarev, G. A. Botton, S. Y. Savrasov, C. J. Humphreys and A. P. Sutton, *Physical Review B*, 1998, **57**, 1505–1509.

[S9] T. Miyake, P. H. Zhang, M. L. Cohen and S. G. Louie, *Physical Review B*, 2006, **74**, 245213.

[S10] Z. Nourbakhsh, *Physica B-Condensed Matter*, 2010, **405**, 4173–4187.

[S11] P. Li, S. H. Deng, L. Zhang, G. H. Liu and J. Y. Yu, *Chemical Physics Letters*, 2012, **531**, 75–79.

[S12] J. P. Tang, L. L. Wang, W. Z. Xiao and X. F. Li, *European Physical Journal B*, 2013, **86**, 362.

[S13] A. Rohrbach, J. Hafner and G. Kresse, *Journal of Physics-Condensed Matter*, 2003, **15**, 979–996.

[S14] S. J. Youn, B. I. Min and A. J. Freeman, *Physica Status Solidi B-Basic Research*, 2004, **241**, 1411–1414.

[S15] C. Franchini, R. Podloucky, J. Paier, M. Marsman and G. Kresse, *Physical Review B*, 2007, **75**, 195128.

[S16] H. Raebiger, S. Lany and A. Zunger, *Physical Review B*, 2009, **79**, 165202.

[S17] H. J. Monkhorst and J. D. Pack, *Physical Review B*, 1976, **13**, 5188–5192.

[S18] C. L. Fu and K. M. Ho, *Physical Review B*, 1983, **28**, 5480–5486.

[S19] R. J. Needs, R. M. Martin and O. H. Nielsen, *Physical Review B*, 1986, **33**, 3778–3784.

[S20] P. E. Blöchl, O. Jepsen and O. K. Andersen, *Physical Review B*, 1994, **49**, 16223–16233.

[S21] T. Sambrook, C. F. Smura, S. J. Clarke, K. M. Ok and P. S. Halasyamani, *Inorganic Chemistry*, 2007, **46**, 2571–2574.

[S22] F. D. Murnaghan, *American Journal of Mathematics*, 1937, **59**, 235–260.

[S23] F. Birch, *Physical Review*, 1947, **71**, 809–824.

[S24] A. Togo and I. Tanaka, *Scripta Materialia*, 2015, **108**, 1–5.

[S25] C. J. Fall, N. Binggeli and A. Baldereschi, *Journal of Physics-Condensed Matter*, 1999, **11**, 2689–2696.

[S26] S. B. Zhang and J. E. Northrup, *Physical Review Letters*, 1991, **67**, 2339–2342.

[S27] C. G. Van De Walle, D. B. Laks, G. F. Neumark and S. T. Pantelides, *Physical Review B*, 1993, **47**, 9425–9434.

[S28] C. Freysoldt, B. Grabowski, T. Hickel, J. Neugebauer, G. Kresse, A. Janotti and C. G. Van de Walle, *Reviews of Modern Physics*, 2014, **86**, 253.

[S29] C. Persson, Y. J. Zhao, S. Lany and A. Zunger, *Physical Review B*, 2005, **72**, 035211.

[S30] E. M. Benecha and E. B. Lombardi, *Physical Review B*, 2011, **84**, 235201.

[S31] H. Dixit, N. Tandon, S. Cottenier, R. Saniz, D. Lamoen and B. Partoens, *Physical Review B*, 2013, **87**, 174101.

[S32] A. Janotti and C. G. Van de Walle, *Applied Physics Letters*, 2005, **87**, 122102.

[S33] A. Janotti and C. G. Van de Walle, *Physical Review B*, 2007, **76**, 165202.

[S34] B. Wybourne, *Spectroscopic properties of rare earths*, Interscience Publishers, 1965.

[S35] G. Racah, *Physical Review*, 1942, **61**, 186–197.

[S36] G. Racah, *Physical Review*, 1942, **62**, 438–462.

[S37] G. Racah, *Physical Review*, 1943, **63**, 367–382.

[S38] G. Racah, *Physical Review*, 1949, **76**, 1352–1365.

[S39] K. Binnemans, *Book*, KU Leuven, 1996.

[S40] R. E. Trees, *Physical Review*, 1951, **83**, 756–760.

[S41] G. Racah, *Physical Review*, 1952, **85**, 381–382.

[S42] G. Racah and Y. Shadmi, *Physical Review*, 1960, **119**, 156–158.

[S43] K. Rajnak and B. G. Wybourne, *Physical Review*, 1963, **132**, 280–290.

[S44] D. J. Newman and S. S. Bishton, *Chemical Physics Letters*, 1968, **1**, 616–618.

[S45] D. Newman and B. Ng, *Crystal Field Handbook*, Cambridge University Press, 2007.

[S46] B. R. Judd, *Physical Review Letters*, 1977, **39**, 242–244.

[S47] D. J. Newman, G. G. Siu and W. Y. P. Fung, *Journal of Physics C-Solid State Physics*, 1982, **15**, 3113–3125.

[S48] B. Ng and D. J. Newman, *Journal of Physics C-Solid State Physics*, 1984, **17**, 5585–5594.

[S49] B. Ng and D. J. Newman, *Journal of Chemical Physics*, 1986, **84**, 3291–3296.

[S50] *Python Software Foundation, Python Language Reference, version 2.7.*, http://www.python.org.

[S51] J. A. Nelder and R. Mead, *Computer Journal*, 1965, **7**, 308–313.

[S52] Z. J. Zhang, A. Feng, X. Y. Sun, K. Guo, Z. Y. Man and J. T. Zhao, *Journal of Alloys and Compounds*, 2014, **592**, 73–79.

[S53] Z. X. Qiu, C. Y. Rong, W. L. Zhou, J. L. Zhang, C. Z. Li, L. P. Yu, S. B. Liu and S. X. Lian, *Journal of Alloys and Compounds*, 2014, **583**, 335–339.

[S54] C. Ballhausen, *Introduction to Ligand Field Theory*, McGraw-Hill, 1970.

[S55] K. E. Lawson, *Journal of Chemical Physics*, 1967, **47**, 3627–3633.

[S56] D. T. Palumbo and J. J. Brown, *Journal of the Electrochemical Society*, 1970, **117**, 1184–1188.

[S57] D. T. Palumbo and J. J. Brown, *Journal of the Electrochemical Society*, 1971, **118**, 1159–1164.

[S58] D. Curie, C. Barthou and B. Canny, *Journal of Chemical Physics*, 1974, **61**, 3048–3062.

[S59] S. Koide and M. H. L. Pryce, *Philosophical Magazine*, 1958, **3**, 607–624.

[S60] J. Hubbard, D. E. Rimmer and F. R. A. Hopgood, *Proceedings of the Physical Society of London*, 1966, **88**, 13–36.

[S61] D. J. Newman, B. Ng and Y. M. Poon, *Journal of Physics C-Solid State Physics*, 1984, **17**, 5577–5584.

[S62] S. Shionoya, W. Yen and H. Yamamoto, *Phosphor Handbook*, CRC Press, 2006.

[S63] G. K. Liu, X. Y. Chen, N. M. Edelstein, M. F. Reid and J. Huang, *Journal of Alloys and Compounds*, 2004, **374**, 240–244.

[S64] W. E. Bron, *Physical Review*, 1965, **140**, 2005–2014.

[S65] M. Wagner and W. E. Bron, *Physical Review*, 1965, **139**, A223–A233.

[S66] W. E. Bron and M. Wagner, *Physical Review*, 1965, **139**, A233–A241.